High-sensitivity temperature sensing using an implanted single nitrogen-vacancy center array in diamond

Junfeng Wang,[1] Fupan Feng,[1] Jian Zhang,[1] Jihong Chen,[2] Zhongcheng Zheng,[2] Liping Guo,[2] Wenlong Zhang,[1] Xuerui Song,[1] Guoping Guo,[3] Lele Fan,[4] Chongwen Zou,[4] Liren Lou,[1] Wei Zhu,[1] and Guanzhong Wang[1,*]

[1]*Hefei National Laboratory for Physical Science at Microscale, and Department of Physics, University of Science and Technology of China, Hefei, Anhui 230026, People's Republic of China*

[2]*Accelerator Laboratory, School of Physics and Technology, Wuhan University, Wuhan, Hubei 430072, People's Republic of China*

[3]*Key Laboratory of Quantum Information, CAS, University of Science and Technology of China, Hefei, Anhui 230026, People's Republic of China*

[4]*National Synchrotron Radiation Laboratory, University of Science and Technology of China, Hefei 230029, People's Republic of China*

(Received 25 November 2014; revised manuscript received 12 February 2015; published 6 April 2015)

We presented a high-sensitivity temperature detection using an implanted single nitrogen-vacancy (NV) center array in diamond. The high-order thermal Carr-Purcell-Meiboom-Gill (TCPMG) method was performed on the implanted single NV center in diamond in a static magnetic field. We demonstrated that under small detunings for the two driving microwave frequencies, the oscillation frequency of the induced fluorescence of the NV center equals approximately the average of the detunings of the two driving fields. On the basis of the conclusion, the zero-field splitting D for the NV center and the corresponding temperature could be determined. The experiment showed that the coherence time for the high-order TCPMG was effectively extended, particularly up to 108 μs for TCPMG-8, about 14 times the value 7.7 μs for thermal Ramsey method. This coherence time corresponded to a thermal sensitivity of 10.1 mK/Hz$^{1/2}$. We also detected the temperature distribution on the surface of a diamond chip in three different circumstances by using the implanted NV center array with the TCPMG-3 method. The experiment implies the feasibility of using implanted NV centers in high-quality diamonds to detect temperatures in biology, chemistry, materials science, and microelectronic systems with high sensitivity and nanoscale resolution.

DOI: 10.1103/PhysRevB.91.155404 PACS number(s): 81.05.ug, 61.72.jn, 07.20.Dt

In recent years some thermal detection techniques have been developed to map temperature distribution with spatial resolution down to the micrometer-nanometer range [1], such as Raman spectroscopy [1,2], fluorescence thermography [1,3], and scanning thermal microscopy [4]. However, such techniques are reported with limitations such as low sensitivity [1,2] and large random errors come from fluorescence rate fluctuations or fluorescence blinking and bleaching in the local environment [1–3]. Recently the negatively charged nitrogen-vacancy (NV^-) center in diamond [5–10] and the spin defects in silicon carbide [11] have been investigated as promising nanoscale temperature sensors with both high temperature precision and high spatial resolution [8–10].

The NV center is a spin defect consisting of a substitutional nitrogen impurity adjacent to a carbon vacancy in diamond. It has increasingly attracted attention in recent years owing to its excellent properties, such as photostability, biocompatibility, chemical inertness, and long spin coherence and relaxation times (∼ms in the isotopically pure diamond) at room temperature. These remarkable properties have been explored in many applications such as quantum information processing [12–16], metrologies such as magnetic field sensing [17–19], electric field sensing [20,21], thermal sensing [8–10], single electron and nuclear spin sensing [22–24], and external nuclear spin sensing [25–27]. In thermal sensing, Neumann *et al.* demonstrated the measurement of the temperature distribution on a glass coverslip using single NV center nanodiamonds as temperature sensors [9]. However, the thermal sensitivity was unsatisfactory due to the short coherence time. To address the short coherence time issue, Toyli *et al.* proposed the thermal Carr-Purcell-Meiboom-Gill (TCPMG) method and extended the spin coherence time up to 17 μs by TCPMG-2 [8].

For further increasing the spin coherence time for the thermometry, in this work, we first studied the effects of the higher order TCPMG method applied on the implanted single NV centers in diamond at room temperature. In particular, a coherence time of 108 μs was obtained for TCPMG-8, about 14 times the value of 7.7 μs for the thermal Ramsey (T-Ramsey) method. This value corresponds to a thermal sensitivity η of 10.1 mK/Hz$^{1/2}$, which is comparable with that of the native NV center in isotopically pure diamond [9,10]. Then we measured the temperature distribution on the surface of a high-purity diamond in three different circumstances by performing the TCPMG-3 pulse sequence measurement on the implanted NV center array. The obtained thermal sensitivity η reached 24 mK/Hz$^{1/2}$. The results demonstrate that the TCPMG method can effectively extend the spin coherence time of the implanted NV center, which paves the way for using the implanted NV center in high-quality nanodiamonds [28] for practical temperature detection with nanoscale resolution and high sensitivity.

The ground state of the NV^- is a spin triplet ($S = 1$), consisting of three spin projection states $|m_S = 0\rangle$ and $|m_S = \pm 1\rangle$, which are split under spin-spin interactions, exhibiting a zero-field splitting $D = 2\pi \times 2.87$ GHz at room temperature. The spin states can be spin polarized and read out optically, and coherently controlled by microwave pulses. The principle of temperature detection using the NV center is based on the temperature dependence of the zero-field splitting D, which

*gzwang@ustc.edu.cn

depends on the local lattice expansion induced by the temperature variation [5–7]. In particular, as has been reported, the value of D is linearly dependent on the temperature with $dD/dT = -74.2$ kHz/K at the temperature from 280 K to 330 K [5].

The scheme of the NV thermometry setup in our experiments is shown in Fig. 1(a). The implanted NV center array in the high-purity diamond was used to sense local temperature on the diamond surface layer. The wavy green arrow represents the 532 nm optical excitation laser which was used to polarize and read out the NV center spin states, and the wavy red arrow represents the emitted fluorescence of the NV center. A 20 μm copper wire was placed on the diamond for transmitting microwaves to manipulate the spin states of the NV center and a 40 μm Nichrome wire placed beside the copper wire was heated by a precision dc power source for sample temperature control. An electromagnet generated an axial magnetic field (32 G) for all the experiments.

The sample was a $2 \times 2 \times 0.5$ mm^3 (100) high-quality electronic grade diamond with natural isotopic concentration of ^{13}C (1.1%) from Element Six ([N] < 5 ppb). The NV center array was made by implanting 60 keV $^{14}N_2^+$ molecules with the fluence 2.25×10^{11} $^{14}N_2^+$/cm^2 and the implantation angle 7° through 45 nm diameter apertures patterned using electron beam lithography in a 300-nm-thick polymethyl methacrylate (PMMA) layer deposited on the diamond surface [29]. The average depth of the NV centers was about 40 nm and the longitudinal and lateral straggling were about 11 and 9 nm, respectively, inferred from SRIM simulations. After implantation, the sample was annealed at 1050 °C in a vacuum at 2×10^{-5} Pa for 2 h to induce vacancy diffusion to form NV centers. Annealing at this temperature could also reduce the total concentrations of the paramagnetic residual defects to extend spin coherence times [30]. After oxidation at 430 °C in atmosphere for 2.5 h for improving negatively charged NV centers' conversion efficiency, the sample was cleaned in a 1:1:1 boiling mixture of sulfuric, nitric, and perchloric acid at 200 °C for one hour. By sampling the NV centers on 194 implanted sites, the mean value was 0.9. Accounting for the irradiation dose of about an average of 6 nitrogen atoms per spot, the generation efficiency of the NV center implantation was about 15%. In such a system, the Hamiltonian of the NV center can be expressed as [8]

$$H = D(T)S_z^2 + g\mu_B \vec{B} \cdot \vec{S} + \vec{S} H_{B1} + H_{B2}, \qquad (1)$$

where $\vec{S}$ is the NV center's electronic spin, $g = 2.00$ is the electron g factor, μ_B is the Bohr magneton, and $\vec{B}$ is the applied magnetic field. The third term describes hyperfine coupling of the NV center spin to the bath of ^{13}C spins, and the last term describes the internal dynamics of the ^{13}C nuclear spin bath. In general, the zero-field splitting parameter $D(T)$ depends on temperature T, axial electric field, and strain. For temperature detection based on $D(T)$, we resonantly manipulate the spin states such that the unwanted relative phase is canceled, getting the common phase factor e^{-iDt}, with the phase proportional to D only. This detection produces a fluorescence intensity (I_{PL}) oscillating between I_{PL} ($m_S = 0$) and I_{PL} ($m_S = \pm 1$) with the frequency given by $|D - \omega|$, where ω is the microwave carrier frequencies used for spin manipulation [8]. When the change of oscillation frequency is determined, the change of D and hence the corresponding local temperature change can be deduced.

We applied the T-Ramsey, thermal echo (TE), and TCPMG-N methods to the implanted NV centers for temperature sensing under finite axial magnetic fields. In these experiments, two microwave radiation fields with different frequencies ω_{-1} and ω_{+1}, in general, are used to manipulate the transitions of $|0\rangle \rightarrow |-1\rangle$ and $|0\rangle \rightarrow |+1\rangle$, respectively. To induce oscillations in $I_{PL}(t)$, both the microwave carrier frequencies are slightly detuned from the corresponding resonance frequencies. The I_{PL} as a function of the free evolution time t follows the equation [8]

$$I_{PL} = a \exp\left[-\left(\frac{t}{T_D}\right)^n\right] \cos(2\pi f t + \varphi) + b, \qquad (2)$$

where a, n, φ, and b are free parameters, and T_D is the thermal pulse sequence coherence time. It is proved that the oscillation frequency $2\pi f = |(\omega_{-1} + \omega_{+1})/2 - D|$ (see Appendix). So we can deduce the coherence time T_D and oscillation frequency f (hence the zero-field splitting D) by fitting the recorded $I_{PL}(t)$ to Eq. (2).

For the T-Ramsey experiment as shown in Fig. 1(d) [9], the spin was first initialized into a superposition state $(|0\rangle + |-1\rangle)/\sqrt{2}$ by a $(\pi/2)_{-1}$ pulse. After half of the total evolution time, a triple echo pulse sequence of the form $\pi_{-1}\pi_{+1}\pi_{-1}$ was applied to swap the population of the $|+1\rangle$ and $|-1\rangle$ states, where the π_{-1} and π_{+1} were the π pulses applied to manipulate the $|0\rangle \rightarrow |-1\rangle$ and $|0\rangle \rightarrow |+1\rangle$ transition, respectively [8,9]. After another half of the total evolution time, the relative phases between the $|0\rangle$ and $|-1\rangle$ states were canceled, getting a total phase factor e^{-iDt}, which was only related to D, independent of low-frequency magnetic noise. We got a coherence time of 7.7 μs for the T-Ramsey sequence, which was larger than the values of 1–5 μs for nanodiamonds [9]. The reason was that, for nanodiamonds, the spin bath contains nuclear spins (^{13}C), high concentration of electron spins ([N] about 100 ppm), and surface layer spins [31,32].

For the TE [Fig. 1(e)] and TCPMG-N experiments [Fig. 2(a)], the working principles are similar to that of the T-Ramsey experiment [8]. We focus on extending the time scale of the first coherence collapse, because our three-level pulse protocols lead to three incommensurate ^{13}C precession frequencies that do not produce the coherence revivals observed in the two-level Hahn echo [8,33]. The key difference between TE and TCPMG-N is that the TCPMG-N experiments invert the spin more frequently (2N times) and hence more effectively eliminate higher frequency magnetic noise, and thus can extend the spin coherence time for thermometry [8]. By fitting the experimental results of the TE and TCPMG-N to the Eq. (2), the coherence times for thermometry were derived. The coherence time of the TE measurement was 9.5 μs, which was close to a value of 10.5 μs obtained from the spin echo experiment [8] [Fig. 2(e)].The TCPMG-1 [Fig. 2(b)] and TCPMG-8 [Fig. 2(c)] experiments extended the coherence time to 14.9 μs and 107.8 μs, respectively. The coherence time of TCPMG-8 was about fifteen times longer than that of the T-Ramsey. Utilizing the obtained experimental data, the corresponding thermal sensitivity of the NV center η can be

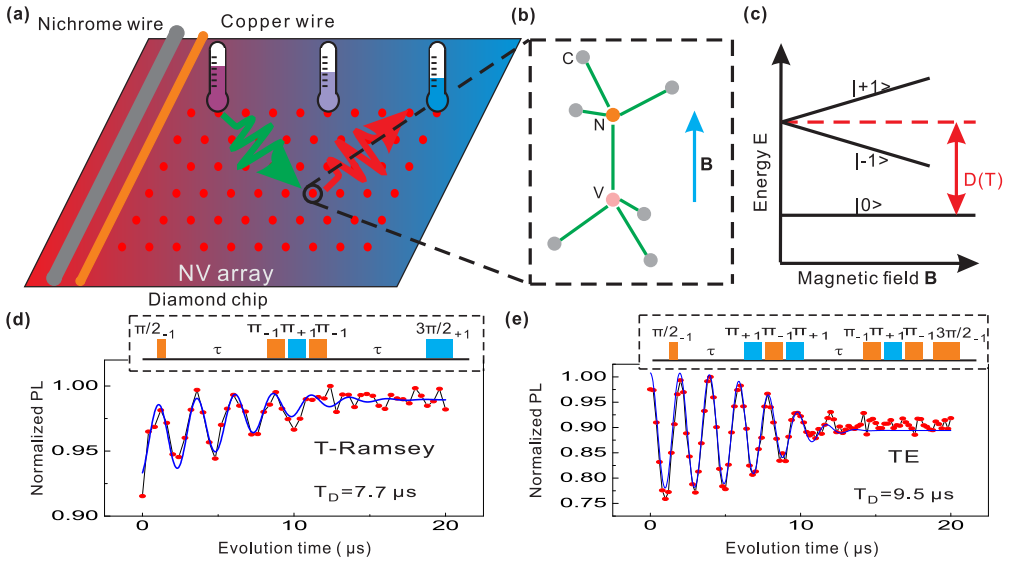

FIG. 1. (Color online) The schematic of the NV center thermometry setup and the thermal pulse sequence measurements. (a) The schematic of the NV center thermometry setup. The implanted NV center array (red points) in a high-purity diamond surface layer was used to sense local temperatures. (b) Atomic structure of a nitrogen (N)–vacancy (V) center in diamond with an arrow indicating the applied axial magnetic field B (32 G). (c) Ground state spin energy levels are split in applied axial magnetic field B. (d) Thermal Ramsey measurement in an axial magnetic field. The inset is the pulse sequence. The coherence time for temperature sensing was 7.7 μs. (e) Thermal echo measurement in an axial magnetic field. The inset is the pulse sequence. The coherence time for temperature sensing was 9.5 μs. The blue lines are the fits to the data; the coherence times are noted on the plots.

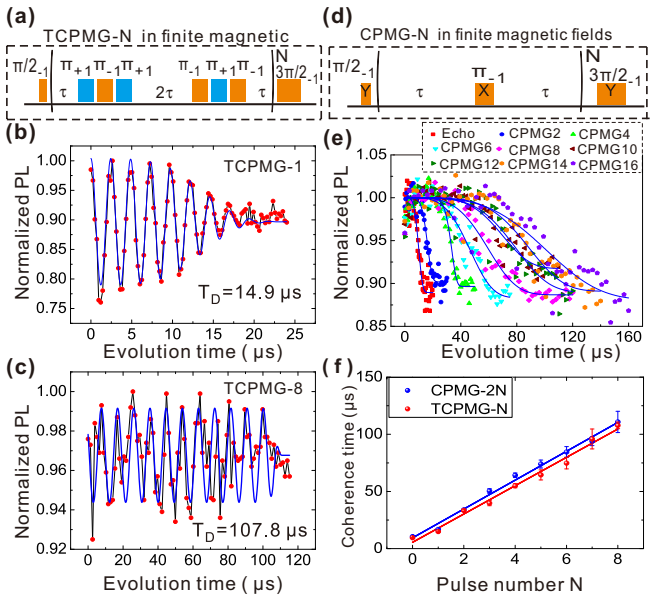

FIG. 2. (Color online) TCPMG-N and CPMG-N pulse sequence measurements in an axial magnetic field. (a) The TCPMG-N pulse sequences. (b) The TCPMG-1 measurement. The coherence time for temperature sensing was 14.9 μs. (c) The TCPMG-8 measurement. The coherence time for temperature sensing was 107.8 μs. (d) The CPMG-N pulse sequences. (e) The coherence decay curves of the Hahn echo and CPMG-N of an N from 2 to 16. The coherence time of the CPMG-16 was 110.8 μs, which was ten times longer than that for spin echo (10.5 μs). (f) The comparison of the coherence time of the TCPMG-N and CPMG-2N for the same number N. Both were linearly increasing with N. The blue and red points at $N = 0$ denote the results for spin echo and TE, respectively.

derived from the following equation [8]:

$$\eta = \sqrt{\frac{2(p_0 + p_1)}{(p_0 - p_1)^2}} \frac{1}{2\pi \frac{dD}{dT} \exp\left[-\left(\frac{t}{T_D}\right)^n\right]\sqrt{t}}, \qquad (3)$$

where p_0 and p_1 are the photon counts per measurement shot for the bright and dark spin states, respectively. In the experiments, we used the oil objective (NA = 1.4) and the obtained p_0 and p_1 values were about 0.029 and 0.02, respectively. Thus the derived thermal sensitivity η of the TCPMG-8 was 10.1 mK/Hz$^{1/2}$, which was comparable with that of the native NV center in isotopically pure diamond [9,10].

Furthermore, the TCPMG method was compared with the conventional CPMG method. In the CPMG-N experiments, as illustrated in Fig. 2(d), the microwave pulse phases of the beginning $(\pi_Y/2)_{-1}$ and the final $(3\pi_Y/2)_{-1}$ pulses were Y phases, while the phases of the echo pulses π_{-1} were X phases [34]. The coherence times obtained in the CPMG-N experiments [Fig. 2(e)] were increasing with the π pulse number N, and, in particular, the T_2 of the CPMG-16 was 110.8 μs, about ten times longer than the value 10.5 μs for the Hahn echo. Considering the fact that there are two triple π pulses in a period of TCPMG, it would be more reasonable to compare TCPMG-N with CPMG-2N. Figure 2(f) shows the obtained dependence of the coherence times for these two methods with the number N. It was found that in both cases the coherence times increased almost linearly with N. This phenomenon of the CPMG was similar to that for the native NV center in high-purity diamond [34], but different from the $N^{2/3}$ dependence in low-purity diamond [35]. It was also noted that the coherence times of TCPMG-N were a little shorter than that in the CPMG-2N, which might be caused by the pulse

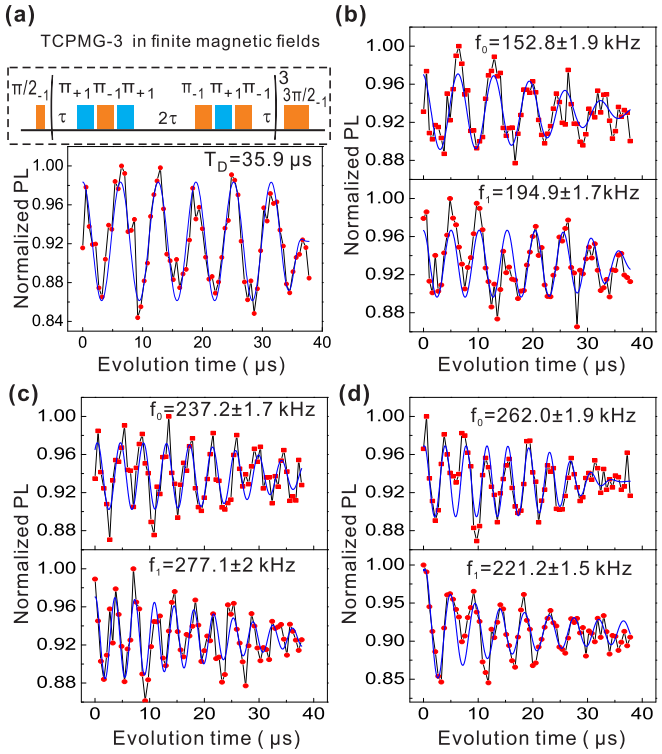

FIG. 3. (Color online) Temperature detection based on the TCPMG-3 pulse sequence in an axial magnetic field. (a) The TCPMG-3 measurement in magnetic field. (b), (c), and (d) show the results under three different microwave detunings, measured with the same heating power on the Nichrome wire. (b) and (c) correspond to two different positive detunings from D and (d) corresponds to a negative detuning from D. The f_0 is the oscillation frequency in a case without heating, and f_1 is the oscillation frequency with heating. For all the TCPMG-3 experiments, each data point represents 2×10^5 averages. The measurement time per point was about 9 s, and total time was about 10 minutes.

imperfections, including pulse length, frequency imperfection, and power fluctuation, since the TCPMG sequences were composed with more microwave pulses.

We now discuss, in more detail, the temperature detection through measuring the changes in the I_{PL} oscillation frequency by applying TCPMG-3 on implanted NV centers. In Fig. 3(a), the upper part shows the pulse sequence of TCPMG-3 and the bottom part shows the results of the TCPMG-3 measurement on a NV center. The coherence time and the oscillation frequency, obtained from fitting the results to Eq. (2), were 159.0 ± 1.0 kHz and 35.9 ± 1.2 μs, respectively. In the experiments, we used the dry objective (NA $= 0.9$) and the obtained p_0 and p_1 values were 0.022 and 0.017, respectively. The corresponding thermal sensitivity η was derived from Eq. (3) to be 24 mK/Hz$^{1/2}$, which was about 6 times improvement in comparison with that for the single NV center nanodiamonds [9]. Furthermore, the relation between the change of the I_{PL} oscillation frequency and the microwave frequency detunings was examined. Figures 3(b)–3(d) show the results for the sample both with and without heating, obtained under three different detunings but the same heating condition. As shown in Figs. 3(b) and 3(c), the changes of I_{PL} oscillation frequency f of the two different positive detunings (both of the microwave carrier frequencies were larger than the corresponding resonance frequencies), were 42.1 ± 2.5 kHz and 39.9 ± 2.6 kHz, respectively, while for the negative detuning (both of the microwave carrier frequencies were less than the corresponding resonance frequencies), it was 40.8 ± 2.4 kHz [see Fig. 3(d)]. It can be seen that the changes of the oscillation frequency f were nearly the same. This result indicates that the change in oscillation frequency depends only on the change in temperature, regardless of the microwave frequencies. This is consistent with the theory described by Eq. (2). Using the standard error derived from the fitting, we estimate that the temperature precision was about 34 mK.

To demonstrate detection of temperature distribution, the implanted NV center array in the surface layer of a diamond chip was used, with which the corresponding local temperatures were measured using TCPMG-3. Figure 4(a) shows the confocal microscope fluorescence image of an area of the sample with an implanted single NV center array in its surface layer. The nearest separation of two NV centers was 2 μm. The larger bright specks in the image were NV center clusters formed during the implantation due to imperfect PMMA templet layer deposited on the diamond chip. The sample was equipped with a Nichrome wire heater, which was situated above the diamond surface [Fig. 1(a)] and arranged parallel to the Y axis. Five single NV centers [named NV-A through E in Fig. 4(a)] with their axes parallel to an axial magnetic field were selected to detect the local temperatures in the diamond surface layer. For all five NV centers, the coherence time of the TCPMG-3 was about 35 μs. In the experiment the sample was situated in air or in oil (Nikon microscope immersion oil). First, we detected the temperatures at four positions in the surface layer of the diamond chip in air (the Nichrome wire was placed 15 μm above the surface of the diamond chip). Figure 4(b) shows the local temperatures detected by the NV-D (273 μm away from the Nichrome wire) at various dc heating powers. It can be seen that the temperature increased sharply at the beginning when the heating power was low, then linearly increased as the dc heating power increased. The sharp increase at the beginning might be due to that the heat dissipation to the environment was less remarkable as the temperature difference between the sample and the surroundings was small at low heating power. On the other hand, as shown in Fig. 4(c), under each dc heating power, the temperatures measured via four NV centers located at different distances from the Nichrome wire were almost the same, even for an NV center 100 μm away from the Nichrome wire. This result can be ascribed to the high thermal conductivity κ of the diamond (about 2000 W/mK). A similar result was obtained by using the same NV-D (289 μm away from the Nichrome wire, Nichrome wire 23 μm above the surface of the diamond chip) with the diamond chip in oil [red points in Fig. 4(d)], except that the rate of the temperature variation for the sample in oil was less than that in air (green points). The temperatures of the five single NV centers at different distances from the Nichrome wire for the sample in oil [Fig. 4(e)] were also almost the same under the same dc powers, similar to the case of the sample in air.

Finally, we detected the temperature distribution on the surface layer of the sample in air, but with a heat sink added

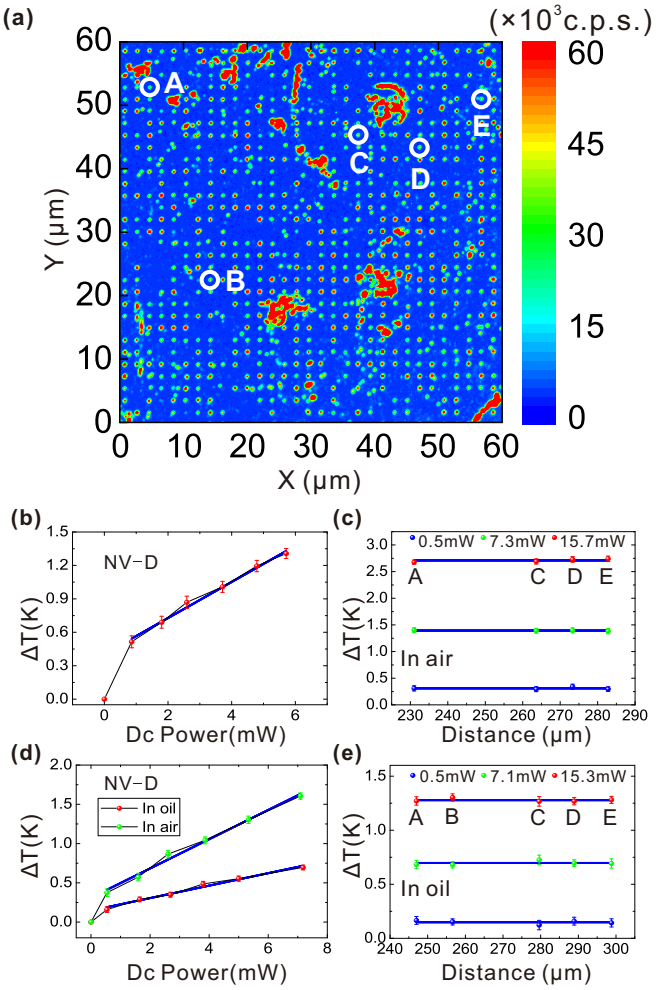

FIG. 4. (Color online) Thermometry using the implanted single NV center array in the diamond chip in air and in oil. (a) Confocal microscope fluorescence image of the implanted NV center array in the high-purity diamond chip. (b) The temperature detected by the center NV-D in the diamond chip in air as a function of the heating power on the Nichrome wire. (c) The temperatures measured by four single NV centers of the chip in air as a function of the distance to the Nichrome wire under three different heating powers. The blue lines for each heating power showed the average temperature value of the four NV centers. (d) The temperature detected by the NV-D as a function of the power on the Nichrome wire for samples in air and oil. (e) The temperatures measured by five single NV centers of the chip in oil as a function of the distance to the Nichrome wire with three different powers. The blue lines for each heating power showed the average temperature value of the five NV centers.

on the other side of the sample [Fig. 5(a)]. The heat sink, a copper wire, was in thermally contacted with a stable heat bath of a temperature 0 °C. The Nichrome heating wire was 20 μm above the surface of the diamond chip. To detect the temperature distribution on the sample surface, nine single NV centers (named NV-A through I, as shown in Fig. 8 and Fig. 9 in the Appendix) were selected to detect the temperatures at the corresponding local positions. The axes of all nine NV centers were parallel to the axial magnetic field and the coherence times measured with TCPMG-3 for these centers were about 35 μs. Figure 5(b) presented a typical dc power dependence

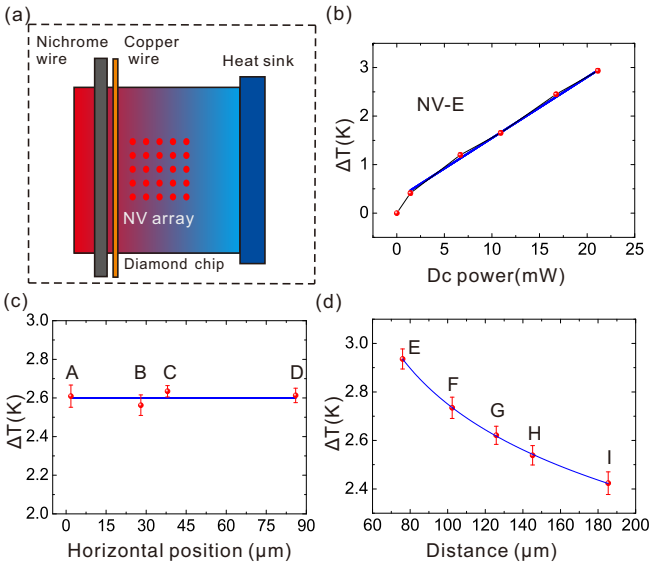

FIG. 5. (Color online) Thermometry using implanted NV center array in the diamond chip, which was located in air and connected to a heat sink. (a) The schematic of the experimental setup for demonstrating the temperature distribution detection. The setup is composed of the diamond chip with an implanted NV center array in it and, as shown in the figure, with a Nichrome heating wire on the left side of the chip and a heat sink on the other side. (b) The temperature detected by NV-E versus the heating power on the Nichrome wire. (c) The temperature distribution along a direction parallel to the Nichrome wire detected by four single NV centers (NV-A through D). The blue line demonstrates that the temperature was nearly the same along the direction parallel to the Nichrome wire. (d) The temperature distribution along a direction perpendicular to the Nichrome wire detected by five single NV centers (NV-E through I). The blue line is the fitting of the experimental data.

of the temperature recorded by NV-E (76 μm away from the Nichrome wire), showing a relationship similar to that for the sample without the heat sink. Furthermore, Fig. 5(c) showed the temperatures measured by using four single NV centers, NV-A through D, that were located at about the same distance (about 96 μm) away from the Nichrome wire with a dc heating power of 20.66 mW. Obviously the temperatures were almost the same, which was in accordance with the geometry of these NV centers: the same distance from the heating wire. However, as shown in Fig. 5(d), the temperatures varied along the perpendicular direction, as represented by temperatures of the five single NV centers, NV-E through I, at different distances to the Nichrome wire that was heated with a dc power of 21.15 mW. According to the steady-state heat conduction equation, the temperature profile on the diamond surface layer follows the expression $\Delta T = a\frac{Q}{\kappa}\ln r + b$, where a, b are free parameters, Q is the heat flux, κ is the thermal conductivity of diamond, and r is the distance between the NV center and the Nichrome wire. It can be seen from the figure that the experimental data were fitted very well with the expression. The experiments showed the effectiveness of the TCPMG method for high-sensitivity temperature detection when performed on the implanted NV centers in high-purity diamond.

In summary, we studied thermometry based on the implanted single NV center in diamond by using the TCPMG

method in a static magnetic field. It was demonstrated that the spin coherence time for thermometry was extended up to 108 μs for TCPMG-8, which was around 14 times the value for the T-Ramsey method (7.7 μs). This value corresponds to a thermal sensitivity 10.1 mK/Hz$^{1/2}$, which is comparable with that for the isotopically pure diamond [9,10]. We measured the temperature distributions on the diamond chip surface in three different circumstances using the TCPMG-3 pulse sequence on the implanted NV center array. The achieved thermal sensitivity was 24 mK/Hz$^{1/2}$, which was about 6 times improvement in comparison with that for the single NV center nanodiamonds [9]. The experiment implies the feasibility for using implanted NV centers in high-quality diamonds to detect temperatures with high sensitivity.

It is expectable that by using higher order TCPMG, isotopically pure diamond, and techniques of higher photon collection efficiency, such as solid immersion lenses [36], the thermal sensitivity can be further improved to sub-mK/Hz$^{1/2}$. Combining the TCPMG method and the implanted NV center in high-purity nanodiamonds [28], high-performance temperature sensors with higher precision, nanoscale spatial resolution, outstanding sensor photostability, and chemical inertness can be constructed, which can be applied to nanoscale temperature detection in a wide variety of systems, including biology [10], chemistry, materials science, and microelectronics systems. The TCPMG thermometry could also be applied to other solid-state quantum spin systems such as point defects in silicon carbide [11,37] for temperature sensing.

We thank Qi Zhang, Fazhan Shi, Pengfei Wang, Jinming Cui, Zhaojun Gong, and Jie You for their help in building the experiment setup and making the sample. We also thank Lei Zhou for his help in the preparation of this paper. This work was supported by the National Basic Research Program of China (2013CB921800, 2011CB921400) and the Natural Science Foundation of China (Grants No. 11374280 and No. 50772110).

APPENDIX:

1. Microwave field frequency detuning and I_{PL} oscillation frequency

We first discuss the oscillation frequency of I_{PL} of a NV center for thermal pulse methods in magnetic field, giving the approximate expression of the oscillation frequency.

The Hamiltonian of the NV center can be expressed as [8]

$$H = DS_z^2 + g\mu_B B S_z + S_z H_{B1} + H_{B2}, \tag{A1}$$

where S_z is the NV center's electronic spin, $g = 2.00$ is the electron g factor, μ_B is the Bohr magneton, and B is the applied magnetic field. The third term describes hyperfine coupling of the NV center spin to the bath of ^{13}C spins, and the last term describes the internal dynamics of the ^{13}C nuclear spin bath. $D = 2\pi \times 2.87$ GHz is the NV center's zero-field splitting.

For an NV center in a magnetic field, the $|-1\rangle$ and $|+1\rangle$ levels of the ground state of the center are split, and the two microwave fields of frequencies ω_1, ω_2 and intensities Ω_1, Ω_2 will be used for driving the two transitions $|0\rangle \rightarrow |-1\rangle$ and $|0\rangle \rightarrow |+1\rangle$, respectively. We will consider the case where the two microwave frequencies are slightly detuned from the corresponding resonance frequencies. The Hamiltonian of the driving field can be expressed as

$$H_{\text{drive}} = \frac{\Omega_1}{2}(|-1\rangle\langle 0|e^{-i\omega_1 t} + |0\rangle\langle -1|e^{i\omega_1 t}) + \frac{\Omega_2}{2}(|+1\rangle\langle 0|e^{-i\omega_2 t} + |0\rangle\langle +1|e^{i\omega_2 t}). \tag{A2}$$

In the rotation frame, the Hamiltonian of the NV center can be expressed as

$$H_{\text{NV}}^R = H_+|+1\rangle\langle +1| + H_-|-1\rangle\langle -1| + H_0|0\rangle\langle 0|, \tag{A3}$$

where $H_- = D - g\mu_B B - \omega_1 - H_{B1} + H_{B2}$, $H_+ = D + g\mu_B B - \omega_2 + H_{B1} + H_{B2}$, and $H_0 = H_{B2}$.

We studied the performances of the three types of thermal pulse sequences: the thermal Ramsey (T-Ramsey), the thermal echo (TE), and thermal CPMG (TCPMG) [8,9]. The general measurement scheme is the same for all of these thermal pulse sequences. After initialization by the first $\pi/2_{-1}$ pulse, the system density matrix is

$$\rho(0) = \tfrac{1}{2}(\mathbf{1} + |0\rangle\langle -1| + |-1\rangle\langle 0|) \otimes \rho_B, \tag{A4}$$

where $\mathbf{1} = (|0\rangle\langle 0| + |-1\rangle\langle -1|)$, and ρ_B is the bath density matrix. The final $3\pi/2_{-1}$ pulse enables us to get the signal $P(t)$ between $\rho(0)$ and $\rho(t)$ as follows:

$$P(t) = \text{Tr}[\rho(0)\rho(t)], \tag{A5}$$

where $\rho(t)$ is the final density matrix after the total evolution time t.

A single period of the TE protocol has the structure [8]

$$\tau - \pi_{+1}\pi_{-1}\pi_{+1} - \tau - \pi_{-1}\pi_{+1}\pi_{-1}, \tag{A6}$$

where the π_{-1} and π_{+1} are the π pulses for driving the $|0\rangle \rightarrow |-1\rangle$ and $|0\rangle \rightarrow |+1\rangle$ transition, respectively, and τ denotes an interpulse delay [8]. So the final density matrix is

$$\rho(t = 2\tau) = \tfrac{1}{2}[\mathbf{1} + U(t)(|0\rangle\langle -1| + |-1\rangle\langle 0|)U(t)^\dagger] \otimes \rho_B, \tag{A7}$$

where the evolution operator $U(t)$ is $U(t) = (\pi_{-1}\pi_{+1}\pi_{-1})U_0(\tau)(\pi_{+1}\pi_{-1}\pi_{+1})U_0(\tau)$, with $t = 2\tau$ and $U_0(\tau) = e^{-iH_{\text{NV}}^R\tau}$.

So we get

$$P(t = 2\tau) = \tfrac{1}{2}(\mathbf{1} + e^{-iH_{B2}^0 2\tau}e^{iH_+\tau}e^{iH_-\tau}|0\rangle\langle -1| + \text{H.c.}), \tag{A8}$$

where H.c. represents the Hermitian conjugate.

We get the TE signal $P(t = 2\tau)$ as

$$P(t = 2\tau) = \frac{1}{2} + \frac{1}{2}\cos\left(\frac{\delta_{-1} + \delta_{+1}}{2}2\tau\right) \times \text{Re}\frac{\text{Tr}_B\left[V_0^2\left(V_{+1}V_{-1}\right)^\dagger\right]}{\text{Tr}_B\mathbf{1}_B}, \tag{A9}$$

where $\delta_{-1} = D - g\mu_B B - \omega_1$ and $\delta_{+1} = D + g\mu_B B - \omega_2$ are two frequency detunings for the $|0\rangle \rightarrow |-1\rangle$ and $|0\rangle \rightarrow |+1\rangle$ transitions, respectively. The Tr_B denotes the trace over

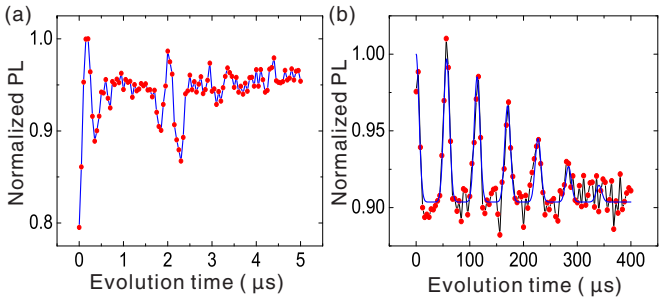

FIG. 6. (Color online) Coherence times of the NV center. (a) Free induction decay (FID) measurement. The T_2^* was about 2.3 μs. (b) Spin echo measurement. The T_2 was 244.1 μs.

the bath, and $\mathbf{1}_B$ is the identity operator in the space of the bath, which ensures correct normalization. The $V_{+1} = e^{-i\tau(H_{B1}+H_{B2})}$, $V_{-1} = e^{-i\tau(-H_{B1}+H_{B2})}$, and $V_0 = e^{-i\tau H_{B2}}$ are three different decoherence factors [8]. So the oscillation frequency f can be expressed as

$$2\pi f = \left|\frac{\delta_{-1}+\delta_{+1}}{2}\right| = |(\omega_{-1}+\omega_{+1})/2 - D|\,. \qquad \text{(A10)}$$

Similarly, for TCPMG-1, the evolution operator $U(t=4\tau)$ is

$$U(t=4\tau) = [U_0(\tau)(\pi_{-1}\pi_{+1}\pi_{-1})U_0(2\tau)(\pi_{+1}\pi_{-1}\pi_{+1})U_0(\tau)]. \qquad \text{(A11)}$$

Following the same procedure as that for TE, we can get the TCPMG-1 signal $P(t=2\tau)$ as

$$P(t=4\tau) = \frac{1}{2} + \frac{1}{2}\cos\left(\frac{\delta_{-1}+\delta_{+1}}{2}4\tau\right) \times \mathrm{Re}\frac{\mathrm{Tr}_B\left[V_0^4(V_{-1}V_{+1}V_{+1}V_{-1})^\dagger\right]}{\mathrm{Tr}_B\mathbf{1}_B}. \qquad \text{(A12)}$$

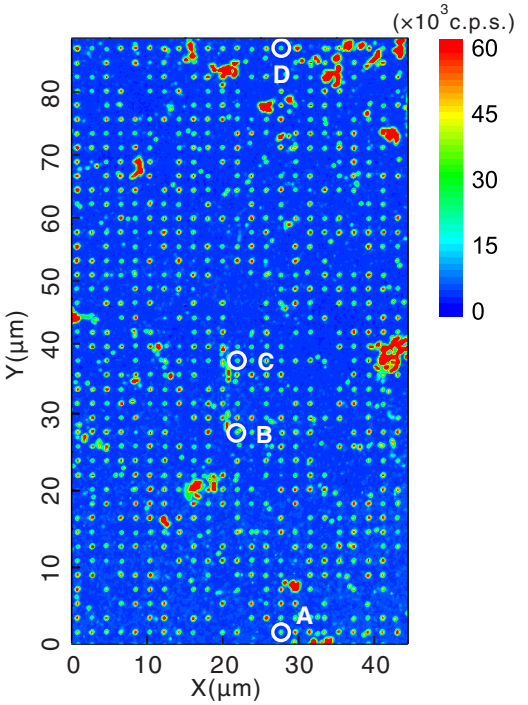

FIG. 8. (Color online) Confocal microscope fluorescence image of the implanted NV center array for detecting temperature distribution along a direction parallel to the Nichrome wire.

It can be seen that the same expression of the oscillation frequency $2\pi f = |(\omega_{-1}+\omega_{+1})/2 - D|$ is obtained for TCPM-1, which is also the same to for the TCPMG-N and T-Ramsey.

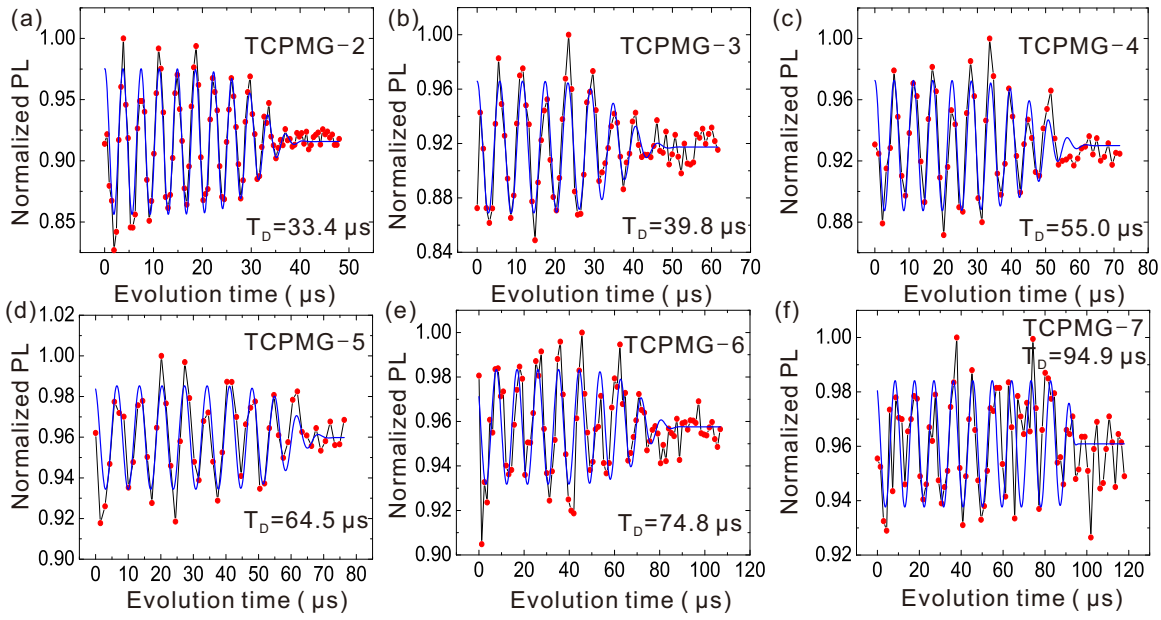

FIG. 7. (Color online) TCPMG-N measurements. (a)–(f) show the measurements of TCPMG-2 through 7, respectively. The blue lines are the fitting based on Eq. (2) in the main text.

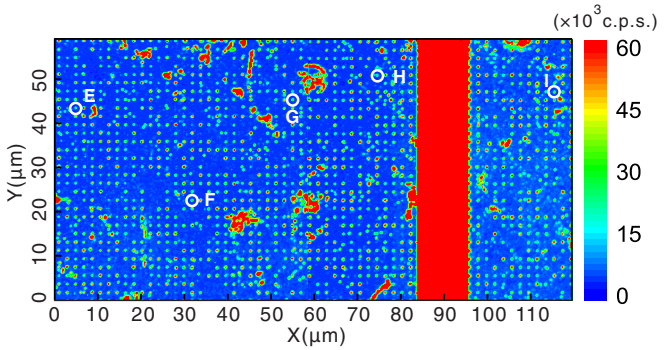

FIG. 9. (Color online) Confocal microscope fluorescence image of the implanted NV center array for detecting temperature distribution along a direction perpendicular to the Nichrome wire.

2. Supplementary information to the TCPMG measurements

We used the same NV center for the experiments corresponding to Fig. 1 and 2. For the center, $T_2^* = 2.3$ μs and $T_2 = 244.1$ μs were measured by free induction decay (FID) and spin echo, respectively, as shown in Fig. 6.

The measurement results for TCPMG-2 through 7 are shown in Fig. 7. From these results, we can infer that the coherence times were increased with the period number N.

3. Confocal microscope fluorescence images of the NV center array used in temperature detections in Fig. 5

The confocal microscope fluorescence image of the implanted NV center array [Fig. 5(c)] for detecting temperature distribution along a direction parallel to the Nichrome wire detected by four single NV centers (NV A through D) is shown in Fig. 8. The confocal microscope fluorescence image of the implanted NV center array [Fig. 5(d)] for detecting temperature distribution along a direction perpendicular to the Nichrome wire by five single NV centers (NV E through I) is shown in Fig. 9. The 10-μm-wide bright strip was due to NV centers formed during the implantation on the lithographic strip on the PMMA templet layer, which was used as the NV center position mark.

4. Influences of the magnetic fields generated by the current in the Nichrome wire

Now, we consider the influences of the magnetic fields generated by the current in the Nichrome wire. The maximum current of the Nichrome wire was about 0.036 A, and the shortest distance of the NV center, used in the experiment, to the wire was about 76 μm. Therefore, the maximum magnetic field generated was about 0.95 G. The effect of the longitudinal component of the magnetic field was eliminated by the decoupling scheme [8–10]. And the transverse magnetic fields will produce shifts in D of a magnitude $(g\mu_B B_T)^2/(2D)$, where B_T is the transverse magnetic fields [8]. For the present condition, the maximum shifts in D were less than 1.3 kHz. So we neglected the effects of thus generated magnetic fields in our experiments.

In addition, the temperature increments of the sample produced by the laser and the microwave used in the experiment can be estimated to be about 3 mK and 1 mK [9], respectively, which can also be neglected in our experiments.

5. Thermal echo measurement at zero magnetic field

We also performed the thermal echo at zero magnetic field on a NV center. At zero magnetic field, by applying a thermal echo (TE) pulse sequence [8,10], as shown in the inset of the Fig. 10(a), the electronic spin of the NV center was first initialized to a superposition state by a $\pi/4$ pulse. After half the total evolution time, a π echo pulse was used to reverse the population of the $|+1\rangle$ and $|-1\rangle$ states. After another half of the total free evolution time, the relative phases between the $|\pm1\rangle$ levels, caused by quasistatic fluctuations of magnetic field, were canceled, getting the common phase factor e^{-iDt}, with the phase proportional to D. As shown in Figs. 10(a), 10(c), and 10(e), spare sampled data made the oscillations difficult to distinguish from the noise in TE measurements with different frequency oscillations because the amplitude of the oscillation induced by the microwave detunings is small [shown in Figs. 10(b), 10(d), and 10(f) in short-time TE measurements]. This might be attributed to that the implanted NV center couples with many paramagnetic defects (implanted N and paramagnetic residual defects) that produce different frequency oscillations [8,10,30]. Therefore, we could not observe a clear oscillation because of the interference between the different frequency oscillations. In addition, the TE sequence produced a long coherence time of about 55 μs, which was much larger than that of the TE in a magnetic field. The reason was that the spin coherence time is limited by the incoherent precession of the ^{13}C nuclei for our natural ^{13}C abundance diamond sample, which causes the coherence to collapse and revive at the ^{13}C Larmor frequency [38]. We focus on extending the time scale of the first coherence collapse in a magnetic field, because our three-level pulse protocols lead to three incommensurate ^{13}C precession frequencies that do not produce the coherence revivals observed in the two-level Hahn echo [8,30]. The spin coherence time of the first collapse decreases with the increasing of the magnetic field [39].

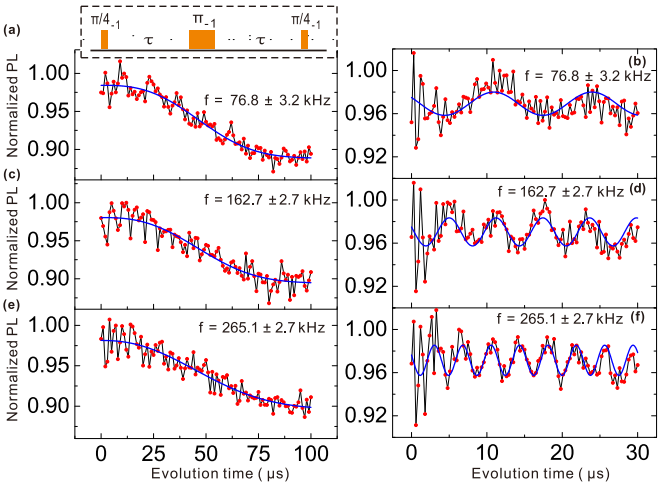

FIG. 10. (Color online) Thermal echo measurements at zero magnetic field with different detunings and evolution times. The inset in (a) is the pulse sequence. The blue lines are the fitting of the I_{PL}.

[1] C. D. S. Brites, P. P. Lima, N. J. O. Silva, A. Millán, V. S. Amaral, F. Palacio, and L. D. Carlos, Nanoscale **4**, 4799 (2012).

[2] A. A. Balandin, S. Ghosh, W. Bao, I. Calizo, D. Teweldebrhan, F. Miao, and C. N. Lau, Nano Lett. **8**, 902 (2008).

[3] G. W. Walker, V. C. Sundar, C. M. Rudzinski, A. W. Wun, M. G. Bawendi, and D. G. Nocera, Appl. Phys. Lett. **83**, 3555 (2003).

[4] A. Majumdar, Annu. Rev. Mater. Sci. **29**, 505 (1999).

[5] V. M. Acosta, E. Bauch, M. P. Ledbetter, A. Waxman, L.-S. Bouchard, and D. Budker, Phys. Rev. Lett. **104**, 070801 (2010).

[6] X. D. Chen, C. H. Dong, F. W. Sun, C. L. Zou, J. M. Cui, Z. F. Han, and G. C. Guo, Appl. Phys. Lett. **99**, 161903 (2011).

[7] D. M. Toyli, D. J. Christle, A. Alkauskas, B. B. Buckley, C. G. Van de Walle, and D. D. Awschalom, Phys. Rev. X **2**, 031001 (2012).

[8] D. M. Toyli, C. F. de las Casas, D. J. Christle, V. V. Dobrovitski, and D. D. Awschalom, Proc. Natl. Acad. Sci. USA **110**, 8417 (2013).

[9] P. Neumann, I. Jakobi, F. Dolde, C. Burk, R. Reuter, G. Waldherr, J. Honert, T. Wolf, A. Brunner, J. H. Shim, D. Suter, H. Sumiya, J. Isoya, and J. Wrachtrup, Nano Lett. **13**, 2738 (2013).

[10] G. Kucsko, P. C. Maurer, N. Y. Yao, M. Kubo, H. J. Noh, P. K. Lo, H. Park, and M. D. Lukin, Nature (London) **500**, 54 (2013).

[11] H. Kraus, V. A. Soltamov, F. Fuchs, D. Simin, A. Sperlich, P. G. Baranov, G. V. Astakhov, and V. Dyakonov, Sci. Rep. **4**, 5303 (2014).

[12] F. Jelezko, T. Gaebel, I. Popa, M. Domhan, A. Gruber, and J. Wrachtrup, Phys. Rev. Lett. **93**, 130501 (2004).

[13] M. V. Gurudev Dutt, L. Childress, L. Jiang, E. Togan, J. Maze, F. Jelezko, A. S. Zibrov, P. R. Hemmer, and M. D. Lukin, Science **316**, 1312 (2007).

[14] P. Neumann, N. Mizuochi, F. Rempp, P. Hemmer, H. Watanabe, S. Yamasaki, V. Jacques, T. Gaebel, F. Jelezko, and J. Wrachtrup, Science **320**, 1326 (2008).

[15] F. Z. Shi, X. Rong, N. Y. Xu, Y. Wang, J. Wu, B. Chong, X. H. Peng, J. Kniepert, R. S. Schoenfeld, W. Harneit, M. Feng, and J. F. Du, Phys. Rev. Lett. **105**, 040504 (2010).

[16] G. Waldherr, Y. Wang, S. Zaiser, M. Jamali, T. Schulte-Herbrüggen, H. Abe, T. Ohshima, J. Isoya, J. F. Du, P. Neumann, and J. Wrachtrup, Nature (London) **506**, 204 (2014).

[17] J. M. Taylor, P. Cappellaro, L. Childress, L. Jiang, D. Budker, P. R. Hemmer, A. Yacoby, R. Walsworth, and M. D. Lukin, Nat. Phys. **4**, 810 (2008).

[18] J. R. Maze, P. L. Stanwix, J. S. Hodges, S. Hong, J. M. Taylor, P. Cappellaro, L. Jiang, M. V. G. Dutt, E. Togan, A. S. Zibrov, A. Yacoby, R. L. Walsworth, and M. D. Lukin, Nature (London) **455**, 644 (2008).

[19] G. Balasubramanian, I. Y. Chan, R. Kolesov, M. Al-Hmoud, J. Tisler, C. Shin, C. Kim, A. Wojcik, P. R. Hemmer, A. Krueger, T. Hanke, A. Leitenstorfer, R. Bratschitsch, F. Jelezko, and J. Wrachtrup, Nature (London) **455**, 648 (2008).

[20] F. Dolde, H. Fedder, M. W. Doherty, T. Nöbauer, F. Rempp, G. Balasubramanian, T. Wolf, F. Reinhard, L. C. L. Hollenberg, F. Jelezko, and J. Wrachtrup, Nat. Phys. **7**, 459 (2011).

[21] F. Dolde, M. W. Doherty, J. Michl, I. Jakobi, B. Naydenov, S. Pezzagna, J. Meijer, P. Neumann, F. Jelezko, N. B. Manson, and J. Wrachtrup, Phys. Rev. Lett. **112**, 097603 (2014).

[22] N. Zhao, J. Honert, B. Schmid, M. Klas, J. Isoya, M. Markham, D. Twitchen, F. Jelezko, R. B. Liu, H. Fedder, and J. Wrachtrup, Nat. Nanotechnol. **7**, 657 (2012).

[23] T. H. Taminiau, J. J. T. Wagenaar, T. van der Sar, F. Jelezko, V. V. Dobrovitski, and R. Hanson, Phys. Rev. Lett. **109**, 137602 (2012).

[24] F. Z. Shi, Q. Zhang, B. Naydenov, F. Jelezko, J. F. Du, F. Reinhard, and J. Wrachtrup, Phys. Rev. B **87**, 195414 (2013).

[25] H. J. Mamin, M. Kim, M. H. Sherwood, C. T. Rettner, K. Ohno, D. D. Awschalom, and D. Rugar, Science **339**, 557 (2013).

[26] T. Staudacher, F. Z. Shi, S. Pezzagna, J. Meijer, J. F. Du, C. A. Meriles, F. Reinhard, and J. Wrachtrup, Science **339**, 561 (2013).

[27] A. O. Sushkov, I. Lovchinsky, N. Chisholm, R. L. Walsworth, H. Park, and M. D. Lukin, Phys. Rev. Lett. **113**, 197601 (2014).

[28] M. E. Trusheim, L. Li, A. Laraoui, E. H. Chen, H. Bakhru, T. Schröder, O. Gaathon, C. A. Meriles, and D. Englund, Nano Lett. **14**, 32 (2014).

[29] P. Spinicelli, A. Dréau, L. Rondin, F. Silva, J. Achard, S. Xavier, S. Bansropun, T. Debuisschert, S. Pezzagna, J. Meijer, V. Jacques, and J.-F. Roch, New J. Phys. **13**, 025014 (2011).

[30] T. Yamamoto, T. Umeda, K. Watanabe, S. Onoda, M. L. Markham, D. J. Twitchen, B. Naydenov, L. P. McGuinness, T. Teraji, S. Koizumi, F. Dolde, H. Fedder, J. Honert, J. Wrachtrup, T. Ohshima, F. Jelezko, and J. Isoya, Phys. Rev. B **88**, 075206 (2013).

[31] A. Laraoui, J. S. Hodges, and C. A. Meriles, Nano Lett. **12**, 3477 (2012).

[32] X. R. Song, J. Zhang, F. P. Feng, J. F. Wang, W. L. Zhang, L. R. Lou, W. Zhu, and G. Z. Wang, AIP Adv. **4**, 047103 (2014).

[33] F. Reinhard, F. Shi, N. Zhao, F. Rempp, B. Naydenov, J. Meijer, L. T. Hall, L. Hollenberg, J. Du, R.-B. Liu, and J. Wrachtrup, Phys. Rev. Lett. **108**, 200402 (2012).

[34] C. A. Ryan, J. S. Hodges, and D. G. Cory, Phys. Rev. Lett. **105**, 200402 (2010).

[35] G. De Lange, Z. H. Wang, D. Ristè, V. V. Dobrovitski, and R. Hanson, Science **330**, 60 (2010).

[36] J. P. Hadden, J. P. Harrison, A. C. Stanley-Clarke, L. Marseglia, Y.-L. D. Ho, B. R. Patton, J. L. O'Brien, and J. G. Rarity, Appl. Phys. Lett. **97**, 241901 (2010).

[37] P. V. Klimov, A. L. Falk, B. B. Buckley, and D. D. Awschalom, Phys. Rev. Lett. **112**, 087601 (2014).

[38] L. Childress, M. V. Gurudev Dutt, J. M. Taylor, A. S. Zibrov, F. Jelezko, J. Wrachtrup, P. R. Hemmer, and M. D. Lukin, Science **314**, 281 (2006).

[39] N. Zhao, S.-W. Ho, and R.-B. Liu, Phys. Rev. B **85**, 115303 (2012).